JACS
JOURNAL OF THE AMERICAN CHEMICAL SOCIETY

ARTICLE

pubs.acs.org/JACS

Evolution of Packing Parameters in the Structural Changes of Silica Mesoporous Crystals: Cage-Type, 2D Cylindrical, Bicontinuous Diamond and Gyroid, and Lamellar

Lu Han,[†] Keiichi Miyasaka,[‡] Osamu Terasaki,[‡,§] and Shunai Che*[,†]

[†]School of Chemistry and Chemical Technology, State Key Laboratory of Composite Materials, Shanghai Jiao Tong University, Shanghai 200240, People's Republic of China

[‡]Graduate School of EEWS (WCU), Korea Advanced Institute of Science and Technology (KAIST) Yuseong Gu, Daejeon 305-701, Republic of Korea

[§]Department of Materials and Environmental Chemistry and Berzelii Center EXSELENT, Stockholm University, S-10691 Stockholm, Sweden

Supporting Information

ABSTRACT: Cage-type, two-dimensional (2D) cylindrical hexagonal (**C**), bicontinuous diamond (**D**), bicontinuous gyroid (**G**), and one-dimensional (1D) lamellar (**L**) structures of silica mesoporous crystals (SMCs) were obtained by using the anionic surfactant *N*-stearoyl-L-glutamic acid (C_{18}GluA) as a template in the presence of the nonionic surfactant $C_{16}(EO)_{10}$ (Brij-56). The mesostructures were controlled by the organic/inorganic interface curvature change induced by Brij-56. A synthesis-field diagram showed that the mesostructure changed in the sequence cage-type → **C** → intergrowth of **C** and **D** → intergrowth of **C** and **G** → **D** → **G** → **L** with increase of the amount of Brij-56. Mixed micelles were formed by the anionic and nonionic surfactants, the packing parameter *g* of which increased with increasing the addition amount of nonionic surfactant and the reaction temperature. The local *g* parameter was obtained from electron crystallography reconstruction results by calculating mean curvatures and Gaussian curvatures from the equi-electrostatic potential surface. The intergrowth of **C** and **D** and two kinds of intergrowth of **C** and **G** are also discussed.

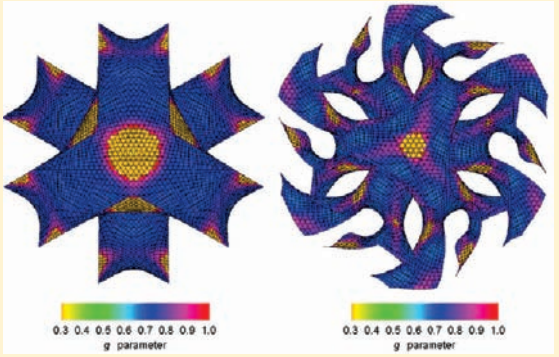

1. INTRODUCTION

Considerable research has been directed toward highly ordered silica mesoporous crystals (SMCs) because their controllable structures and compositions make them suitable for a broad range of applications in catalysis, sorption, controlled drug release, and advanced materials design.[1−3] Although there are many different strategies for the preparation of SMCs, they are often formed upon surfactant or block copolymer micelles as templates for self-assembly and subsequent and/or simultaneous condensation of inorganic precursors.[4] The charge density matching/ion-exchanging between the surfactant and the inorganic precursor and the self-assembly of the surfactant−silica complex are essential for the formation of the mesostructured crystals.[5] The self-assembly of the surfactant−silica complex happened to form silicatropic liquid crystal phases,[6] which are highly relevant to the lyotropic liquid crystals. Compared to the lyotropic liquid crystals formed by amphiphilic molecules in the presence of water, a synthesis-field diagram for SMCs is more complex, and SMCs can be immobilized for further characterization. Liquid crystal phases such as bilayer, cylindrical, and spherical are generally described by a surfactant packing parameter, $g = V/a_0 l$, where V is the surfactant chain volume, a_0 is the effective hydrophobic/hydrophilic interfacial area, and l is chain length.[7] On the basis of this scheme, ideal bilayer, bicontinuous, cylindrical, and spherical geometries have *g* values 1, 2/3, 1/2, and 1/3, respectively. Various SMCs with different structures (hereafter mesostructures) can be formed according to the packing behavior of the surfactants, namely 1D-lamellar, 2D-cylindrical, bicontinuous cubic, micellar cubic, and new types with minimal surfaces.[4,5,8−20]

The 2D cylindrical (**C**) structure is the most common for SMCs.[4,5] Normally, the cylindrical micelles have a circular cross-section and arrange in a 2D hexagonal manner with the plane group *p6mm*. Typical materials are MCM-41, SBA-15, SBA-3, AMS-3, etc. The bicontinuous structures have attracted a great deal of interest because of their complex and highly symmetric structures in which two disconnected but interwoven mesoporous networks divided by a silica wall grow along a continuously curved surface. MCM-48 was the first bicontinuous cubic

Received: January 24, 2011
Published: June 22, 2011

dx.doi.org/10.1021/ja200683t | *J. Am. Chem. Soc.* 2011, 133, 11524–11533

mesoporous solid with space group $Ia\bar{3}d$, and typical SMCs with this structure include KIT-6, FDU-5, AMS-6, etc. Their walls follow a gyroid minimal surface (**G**).[4,11] Recently, we discovered an SMC with typical diamond minimal surface (**D**) with $Pn\bar{3}m$ symmetry in an anionic surfactant-templated mesoporous silica (AMS) system, using a costructure-directing agent (CSDA).[15] In addition, a bicontinuous cubic primitive minimal surface (**P**) with $Im\bar{3}m$ symmetry was prepared by Wiesner et al.[21] A typical example of lamellar structure (**L**) is MCM-50, in which a bilayer composed of surfactant and silica regions is alternatingly interwoven.[4]

Both the **L** ↔ **G** and **G** ↔ **C** transitions have received considerable attention since Rançon and Charvolin reported the epitaxial growth of **C** and **G** phases specially matched in orientation and periodicity in lyotropic liquid crystals.[22−28] The kinetics and mechanisms of the bicontinuous phase transitions have been also widely reported. These minimal surfaces all have genus 3 in their primitive cells and are topologically equivalent. **P**, **G**, and **D** surfaces can be interconverted by Bonnet transformation.[29,30] As described by Hyde,[31] at a given chain packing parameter, small variations in the chain volume fraction (defined as the total apolar fraction of the amphiphilic molecule, including apolar solvents) may cause phase transformations between the different cubic bicontinuous phases. Transitions with increasing chain volume fraction may occur in the sequence **P** → **D** → **G**, but there have been no experimental reports on this transition in SMCs.

In the synthesis system of SMCs, structural changes have also been followed with interest.[17,32,33] It is well-known from experiment that the mesostructure changes from **L** to **C** through **G** and finally to cage-type structure, with decreasing packing parameter. In typical phase diagrams, **G** occurs in a narrow region between **L** and **C**. Moreover, Landry et al. reported that **G** could be obtained by a structural change from **C** with incompletely polymerized mesostructure, followed by an advanced heating step.[32] They also proposed a model to explain the expected **C** to **G** transformation, which is similar to the epitaxial relationship reported for a block polymer solution system.[33] Unfortunately, no experimental evidence for the epitaxial relationship of **C** and **G** or **C** and **D** has been reported.

D is very rare compared to the commonly observed **G** and has been found solely in the AMS synthesis system.[15] In our previous work, we presented a full-scale synthesis-field diagram using the diprotic anionic surfactant *N*-myristoyl-L-glutamic acid (C_{14}GluA) as the template and *N*-trimethoxysilylpropyl-*N*,*N*,*N*-trimethylammonium chloride (TMAPS) as CSDA. The resultant mesostructures changed from cage-type structures to **C** and finally **D** when the ionization of C_{14}GluA was decreased,[17] which is consistent with the change of the geometry of the micelles as described above. **G** (AMS-6) has been synthesized using *N*-lauroyl-L-alanine (C_{12}AlaA) as surfactant and 3-aminopropyl trimethoxysilane (APS) as CSDA.[34] However, **G** cannot be formed by controlling the charge density of the micelle surfaces via differences of ionization of carboxylate surfactants with the diprotic glutamic headgroup.

Very recently, two of us reported a self-consistent structural solution for the SMCs MCM-48 and AMS-10 by combined electron crystallography and curvature assessment.[35] According to the mean curvature and the Gaussian curvature analyses, the local curvature distributions of **D** stay in a narrower range than that of **G**, which means that **D** accommodates smoother silica wall structure. However, up to now **G** and **D** have not been found in a single synthesis system; thus, the structures of **G** and **D** cannot be compared straightforwardly.

Herein we present a synthesis-field diagram of the AMS materials prepared with the amino acid-derived anionic amphiphilic molecule *N*-stearoyl-L-glutamic acid (C_{18}GluA) as template, APS as CSDA, and tetraethyl orthosilicate (TEOS) as silica source, in the presence of nonionic surfactant $C_{16}(EO)_{10}$ (Brij-56). As Brij-56 can be associated with the anionic surfactant micelle, the *g* parameter of the mixed micelle can be well tuned by controlling the amount of Brij-56 added and the reaction temperature. On the basis of this concept, a series of SMCs have been obtained and an unusual structural change involving cage-type, **C**, **D**, **G**, and **L** has been discovered. The structural solutions were obtained using powder X-ray diffraction (XRD), nitrogen adsorption−desorption, scanning electron microscopy (SEM), and high−resolution transmission electron microscopy (HRTEM). The structural relationship with the surface curvature analysis of the mesostructures was investigated. By using electron crystallographic assessment, the actual *g* parameters of **D** and **G** formed in this system were determined and directly compared with one another. In addition, new intergrowth of **C** and **D** and the intergrowth of **C** and **G** were observed and studied in detail.

2. EXPERIMENTAL SECTION

2.1. Chemicals. All materials were used as purchased without further purification. TEOS was obtained from SCRC, China, APS from TCI, Brij-56 from Aldrich, and anionic surfactant C_{18}GluA from Ajinomoto Co., Ltd.

2.2. Synthesis of SMCs. The SMCs were synthesized by using the anionic surfactant as a structure-directing agent, APS as CSDA, and TEOS as silica source, in the presence of Brij-56. In a typical synthesis, C_{18}GluA and Brij-56 were dispersed in deionized water at 80 °C in a 50 mL beaker. After the surfactant mixture was cooled to a designated temperature (i.e., 50 °C), a mixture of TEOS and APS was added rapidly with stirring (∼600 rpm). After 20 min of stirring, the reaction mixture was aged at the same temperature for 2 days under static conditions.

As nanoparticles have been synthesized in most of the cases, it is very difficult to separate the solid products by filtration. Besides, the samples were also difficult to be recovered by centrifugal separation because of the sticky synthesis solution. Thus, the products were frozen in a refrigerator overnight and subsequently freeze-dried, and surfactant-free materials for HRTEM analyses were obtained by calcination at 550 °C in air for 6 h. The various synthesis compositions are shown in Table S1 (Supporting Infomation).

2.3. Characterizations. XRD patterns were recorded with a Phillips PANalytical instrument equipped with monochromator under the conditions $Cu_{K\alpha 1}$ radiation (wavelength 1.5406 Å), 45 kV and 40 mA, in transmission mode at scan rate 0.1° min^{-1} over the range 0.9−6° (2θ). The nitrogen adsorption−desorption isotherms were measured at 77 K with a Quantachrome Nova 4200E instrument. The surface area was calculated by the Brunauer−Emmett−Teller (BET) method, and the pore size was obtained from the pore size distribution curve calculated by the Barett−Joyner−Halenda (BJH) method using the desorption branch of the isotherm. SEM was conducted on a JEOL JSM-7401F electron microscope operated at 1 kV. HRTEM observations were performed with a JEOL JEM-3010 microscope operating at 300 kV (Cs = 0.6 mm, point resolution 1.7 Å). Images were recorded with a charge-coupled device (CCD) camera (Keenview, 1376 × 1096 pixels, pixel size 6.4 μm × 6.4 μm) under low-dose conditions. The sample was crushed in an agate mortar, dispersed in ethanol, and then dropped onto a thin carbon film on a Cu grid.

3. RESULTS AND DISCUSSION

3.1. SMCs Synthesized with Varying Brij-56/C_{18}GluA Molar Ratios at Various Temperatures. Various SMCs with differing organic/inorganic interface curvature have been achieved by using cationic surfactants via S^+I^- and $S^+X^-I^+$ routes, and nonionic surfactants via the S^0I^0 or $(S^0H^+)(X^-I^+)$ synthesis routes. However, only lamellar or disordered mesostructures have resulted from the use of anionic surfactants with (similar to cationic and nonionic surfactant) templating routes of S^-I^+ or $S^-M^+I^-$ (metal counterion mediated).[36] A possible reason is that under acidic conditions an anionic surfactant can be largely protonated, while under basic conditions the interaction of countercations with surfactant and silicate ion is too weak.

In 2003 we reported a new anionic surfactant templating route to highly ordered SMCs by introducing an additional CSDA, and a family of highly ordered SMCs, the AMS-n series, were synthesized under varying conditions.[15−17,34,37−42] Structurally, a CSDA contains two parts, an alkoxysilane site that is capable of being cocondensed with a silica source, e.g., TEOS, and an organic site that can form electrostatic interactions with the headgroups of the surfactant. Thus, the negatively charged headgroups of anionic surfactants interact electrostatically with the positively charged ammonium sites of the CSDAs, providing the driving force for formation of highly ordered mesostructures.

In the CSDA synthesis method, the organic/inorganic interface curvature can be controlled well by the geometry of either the surfactant headgroup or the CSDA part, by simply controlling their ionization through varying the pH of the solution. This is one of the prominent characteristics that differentiates the CSDA method from conventional cationic and nonionic surfactant approaches.[38] The structural change resulting from varying the ionization of the surfactant has been extensively discussed in our earlier papers.[15,17,38] As discussed in the Introduction, **G** cannot be formed by controlling the charge density of the micelle surfaces via differences of ionization of C_{14}GluA with the diprotic glutamic headgroup. Thus, to obtain the whole synthesis-field diagram including both **G** and **D**, a different synthesis strategy is required.

C_{18}GluA, with a long carbon chain and diprotic glutamic headgroup, was chosen. The diprotic headgroup of C_{18}GluA contributes a large effective area to the critical packing parameter. Moreover, the longer chain of C_{18}GluA compared to C_{14}GluA should make it easier to form a mesostructure with a higher *g* parameter if an agent is added to reduce the organic/inorganic interface curvature. In our previous study, SMCs synthesized with C_{18}GluA and varying amounts of APS were studied.[41] It was also found that the nonionic surfactant Brij-56 can form micelles together with diprotic glutamic type anionic surfactant C_nGluA, and the organic/inorganic interface curvature can be tuned by addition of Brij-56 and varying the reaction temperature.[43] For that reason, we used nonionic surfactant Brij-56 in the AMS synthesis system. We fixed the APS/C_{18}GluA ratio at 2 to ensure 1:1 interaction between the diprotic glutamic surfactant headgroup and the CSDA.

Various SMCs with different organic/inorganic interface curvatures were synthesized with Brij-56/C_{18}GluA molar ratios in the range 0−2.0, at various temperatures. The synthesis composition was C_{18}GluA:Brij-56:APS:TEOS:H_2O = 1:*x*:2:15:2335. A number of mesostructures, cage-type, **C**, **D**, **G**, and **L**, were obtained in the synthesis-field diagram (Figure 1). Determination of crystal structures and space groups was carried out on the basis of XRD and TEM observations. All of the samples synthesized without Brij-56 had low-ordering cage-type structures, the same as our previous report.[41] The anionic surfactant C_{18}GluA has two headgroups, which makes the effective headgroup area of the critical packing parameter larger than that of the surfactants normally used for conventional SMCs, leading to the formation of cage-type structures. At 30 °C, with increasing amount of Brij-56 in the synthesis system, structural change from cage-type (Brij-56/C_{18}GluA = 0) to **C** (Brij-56/C_{18}GluA = 0.29−1.75) occurred. At 80 °C, the cage-type structure changed to **L** (Brij-56/C_{18}GluA = 1.45−1.75) through an undefined disordered structure region (Brij−56/C_{18}GluA = 0.29−1.15). Notably, a complicated and exceptional mesostructural transformation was observed from the samples synthesized at 50 °C. The mesostructure evolved with an increase of the Brij-56/C_{18}GluA molar ratio from cage-type (Brij-56/C_{18}GluA = 0) to **C** (Brij-56/C_{18}GluA = 0.29−0.85), to intergrowth of **C** and **D** (Brij-56/C_{18}GluA = 1.15), to intergrowth of **C** and **G** (Brij-56/C_{18}GluA = 1.30), and then to pure **D** (Brij-56/C_{18}GluA = 1.45) and finally to pure **G** (Brij-56/C_{18}GluA = 1.60−1.90). Still higher concentrations of Brij-56 gave highly viscous solutions and failed to produce SMCs of high quality. Because a range of different mesostructures were formed by increasing the Brij-56/C_{18}GluA molar ratio at 50 °C, we subsequently focused on those samples. XRD patterns, SEM images, and HRTEM images of the samples synthesized at 30 °C and 80 °C are shown in the Supporting Information (Figures S1−S6).

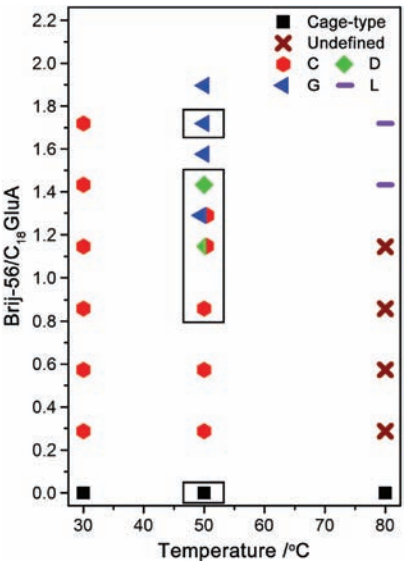

Figure 1. Synthesis-field diagram of the C_{18}GluA/Brij-56/APS synthesis system at various temperatures. The synthesis composition was C_{18}GluA:Brij-56:APS:TEOS:H_2O = 1:*x*:2:15:2335.

Figure 2 shows powder XRD patterns of the calcined SMCs synthesized using varying Brij-56/C_{18}GluA molar ratios at 50 °C (also indicated in Figure 1, the XRD patterns of the as-synthesized SMCs are shown in Figure S7, Supporting Information). Structural determination using these XRD data alone is risky because of the limited number of reflections, so structural analyses were made with the help of HRTEM observations. The sample synthesized without Brij56 showed two peaks in the range of 2θ = 1.5−4°. The powder from the synthesis gels with Brij-56/C_{18}GluA molar ratio 0.85 gave an XRD pattern with one strong peak around 2°, indexed as 10 reflections,

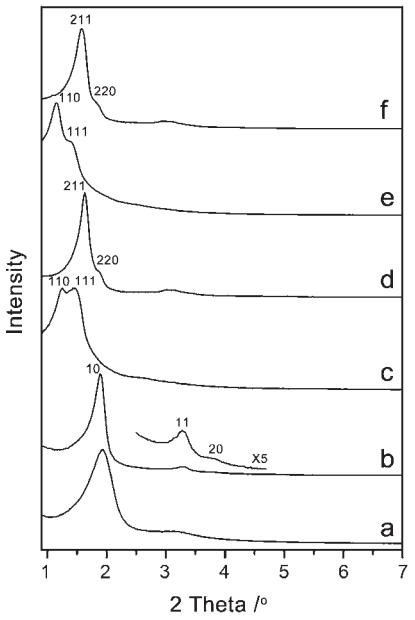

Figure 2. XRD patterns of the sample synthesized with various Brij-56/C_{18}GluA molar ratios at 50 °C. The chemical molar composition of the reaction mixture was as follows. C_{18}GluA:Brij-56:APS:TEOS:H_2O = 1:*x*:2:15:2335, where Brij-56/C_{18}GluA molar ratios were (a) 0, (b) 0.85, (c) 1.15, (d) 1.30, (e) 1.45, and (f) 1.75. The samples are marked in Figure 1. The XRD patterns were recorded on a Phillips PANalytical instrument equipped with $Cu_{K\alpha 1}$ radiation (wavelength 1.5406 Å).

and two additional weak peaks in the range 3−5°, indexed as 11 and 20 reflections, assuming 2D hexagonal *p6mm* mesostructure (**C**) with unit cell parameter a = 5.4 nm. The sample synthesized with Brij-56/C_{18}GluA molar ratio 1.15 gave two intense peaks in the region of 1−2° with d-spacing ratio about $3^{1/2}/2^{1/2}$, which were indexed as 110 and 111 reflections assuming the **D** structure with $Pn\bar{3}m$ symmetry. The sample synthesized with Brij-56/C_{18}GluA molar ratio 1.30 showed a number of well-resolved peaks (2θ = 1.5−4°) with peak positions consistent with **G** with $Ia\bar{3}d$ symmetry. The XRD pattern of the sample synthesized with Brij-56/C_{18}GluA molar ratio 1.45 revealed well resolved peaks with positions in the ratio $3^{1/2}/2^{1/2}$, which is consistent with 110 and 111 reflections of **D**, with unit cell parameter a = 10.8 nm. The XRD pattern of the sample synthesized with Brij-56/C_{18}GluA molar ratio 1.75 showed a pattern similar to that of the sample synthesized with Brij-56/C_{18}GluA molar ratio 1.30, which had a typical **G** structure with unit cell parameter a = 13.6 nm.

All of the calcined samples were further characterized by HRTEM analyses. The sample synthesized without Brij-56 had spherical morphology with diameter 60−80 nm (Figure S8a, Supporting Information). This sample shows low-ordering cage-type structure and small ordered domains of several units cell size can be often observed. Very few TEM images suggest that the large domains have cubic close-packed (CCP) structures (Figure 3a). For the sample synthesized with Brij-56/C_{18}GluA molar ratio 0.85, both top and side views of the hexagonal rods (Figure S8d) with 2D hexagonal structure (**C**) can be observed from the HRTEM image (Figure 3b).

Figure 4 shows HRTEM images of the sample synthesized with Brij-56/C_{18}GluA molar ratio 1.15. Interestingly, most of the particles (Figure S8e) obtained from this synthesis composition

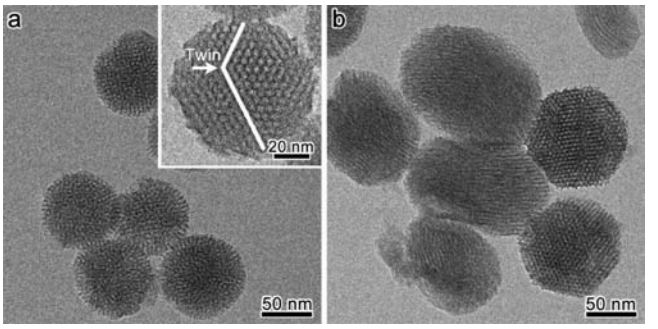

Figure 3. HRTEM images of the sample synthesized with Brij-56/C_{18}GluA molar ratio of (a) 0 and (b) 0.85 at 50 °C. The sample synthesized without Brij-56 shows low-ordering cage-type CCP structure. The inset shows an enlarged particle taken from the [110] axis; a twin plane can be observed. The sample synthesized with a Brij-56/C_{18}GluA molar ratio of 0.85 exhibits 2D hexagonal C structure.

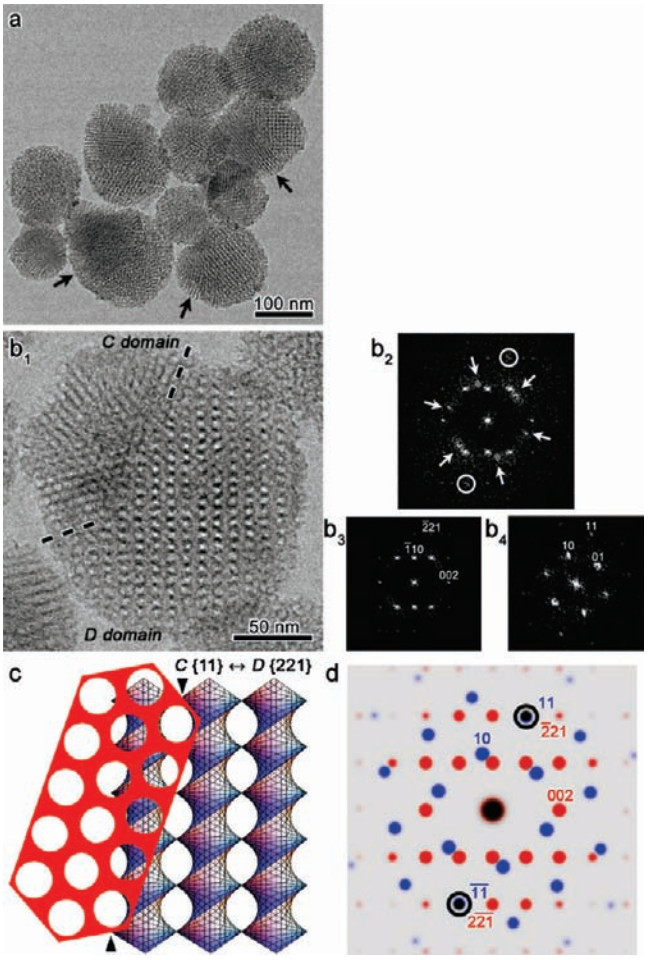

Figure 4. HRTEM images of the sample synthesized with Brij-56/C_{18}GluA molar ratio of 1.15 at 50 °C. (a) Low magnification TEM image and (b_1) intergrowth of **C** and **D** taken along the $[110]_D$ axis, and the corresponding FDs taken from (b_2) the whole particle (the arrows indicate the diffraction spots of **C**), (b_3) the **D** domain, and (b_4) the **C** domain, respectively. (c) A schematic drawing of the observed intergrowth of **C** and **D** and (d) simulated electron diffraction pattern, showing the **C** {11} ↔ **D** {221} transition.

showed an intergrowth texture composed of mesostructures of **C** and **D** (Figure 4a). Figure 4b_1−4b_4 shows an enlarged particle

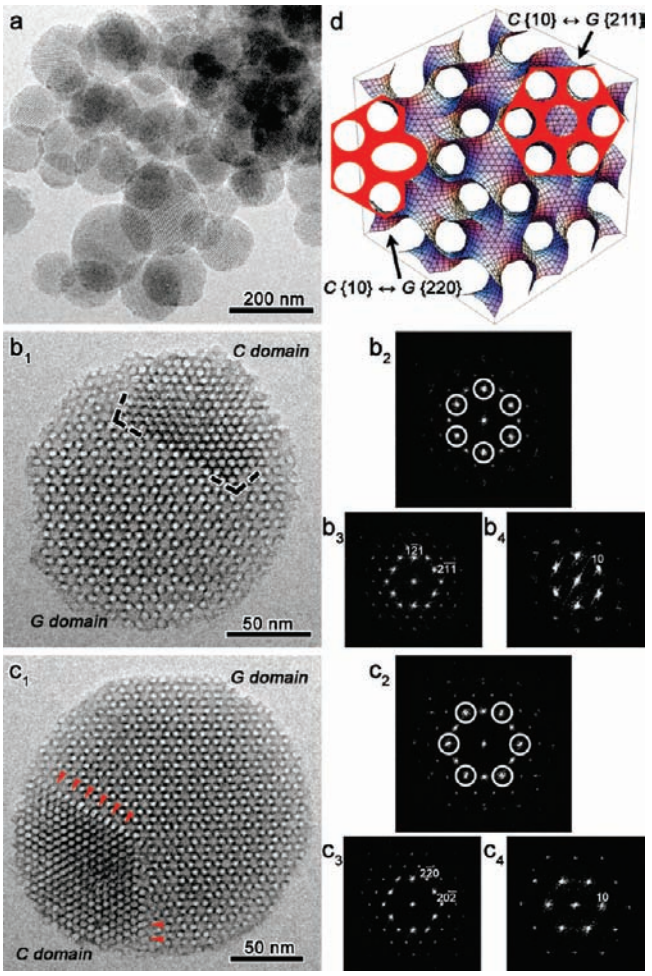

Figure 5. HRTEM images of the sample synthesized with Brij-56/C_{18}GluA molar ratio of 1.30 at 50 °C. (a) Low magnification TEM image, (b_1) intergrowth of **C** {10} ↔ **G** {211} taken along the $[111]_G$ axis and the corresponding FDs taken from (b_2) the whole particle, (b_3) the **G** domain, and (b_4) the **C** domain, respectively. (c_1) Intergrowth of **C** {10} ↔ **G** {220} taken along the $[111]_G$ axis and the corresponding FDs taken from (c_2) the whole particle, (c_3) the **G** domain, and (c_4) the C domain, respectively, and (d) a schematic drawing of the observed intergrowth sites of **C** and **G**.

taken from $[110]_D$ and the corresponding FDs of the whole particle, **D** domain and **C** domain, respectively. The top left part corresponds to a typical top view of **C**, while the right part shows the [110] contrast of **D**. The cylinders of **C** are parallel to the $\langle 110\rangle_D$, showing a "side by side" epitaxial relationship. It is interesting to note that the {11} reflection of **C** overlaps with the {221} reflection of **D** (indicated by white circles in Figure $4b_2$), suggesting a **C** {11} ↔ **D** {221} transition. Figure 4c and 4d shows the 3D representation of the intergrowth structure of the **C** {11} ↔ **D** {221} transition and the simulated electron diffraction pattern, respectively. The $\{11\}_C$ is rotated 19.5° from the $\{110\}_D$, and only one of every four adjoining cylinders of **C** can overlap with the diamond channels of $[110]_D$ at the boundary part similar to a coincidence boundary (indicated by arrowheads in Figure 4c). This is the first time that the epitaxial intergrowth of **C** and **D** has been reported.

The particles (Figure S8f) obtained with Brij-56/C_{18}GluA molar ratio 1.30 showed an intergrowth structure composed of **C** and **G** (Figure 5a). However, from the HRTEM images taken along $[111]_G$ direction, two kinds of connection between **C** and **G** were found (Figure 5b and 5c). Figure $5b_1$ shows one intergrowth relationship: it can be clearly observed from the HRTEM image that the cylinders of **C** are parallel to the $\langle 111\rangle_G$, indicating a "side by side" intergrowth. In addition, there is an obvious boundary between **C** domain and **G** domain with contrast change. The six white dots observed from $\langle 111\rangle_G$, which are the channels surrounded by the gyroid minimal surface, turned into the cylinders of **C** and a new cylinder appeared in the center of the hexagonally arranged **G** channels, where the density of SiO_2 is low. Figure $5b_2-5b_4$ shows the FDs of the whole particle, **G** domain, and **C** domain, respectively, suggesting that the {10} reflection of **C** overlaps with the {211} reflection of **G**, implying a **C** {10} ↔ **G** {211} transition. It is worth noting that $d_{(10)C}$ gradually decreased with distance from the **G** domain and became 4.8 nm (calculated from FD), slightly smaller than $d_{(211)G}$ of 5.2 nm. The other type of intergrowth is shown in Figure $5c_1-5c_4$. In this case, the two domains also follow "side by side" stacking, while the {10} reflection of **C** overlaps with the {220} reflection of **G**, i.e., the **C** {10} ↔ **G** {220} transition. In this case the cylinders of **C** domain cannot fit in the channels of the **G** domain perfectly; thus, numerous defects with elliptical channels were created at the boundary (marked by the red arrows in Figure $5c_1$). It was calculated from FDs that $d_{(10)C}$ = 4.7 nm and $d_{(220)G}$ = 4.6 nm.

Most of the existing experiments and theories support the correlation that the two phases align side by side, with the cylinder axis of **C** equivalent to the body diagonal of **G** with a **C** {10} ↔ **G** {211} transition, as the {211} planes have the highest density.[19−27] Landry et al. suggested a similar relationship for the SMC system.[32,33] The **C** {10} ↔ **G** {220} transition was suggested by Honda et al., owing to the domain spacing satisfying the epitaxial relationship.[24] However, in his structural model, the cylinders of **C** do not overlap with but lie in between the **G** channels. Figure 5d shows a 3D representation of the two types of connections of **C** and **G**: the **C** {10} ↔ **G** {211} transition and the **C** {10} ↔ **G** {220} transition. The *d*-spacings obey the relationship $d_{(220)G} \approx d_{(10)C} < d_{(211)G}$, which may be the reason that the **C** {10} ↔ **G** {220} transition occurs. Compared to the **C** {10} ↔ **G** {211} transition, the cylinders of **C** can still fit the spacing of the **G** channels after 30° rotation. In previous studies, the details of the microscopic dynamics of this epitaxial transition were not observed directly because of limited resolution of the scattering experiments, and the difficulties of direct observation of this intergrowth structure. However, immobilizing lyotropic liquid crystal mesophases in SMCs enables detailed study by the HRTEM technique. The epitaxial relationship of the mesostructures can thus be observed directly and confirmed experimentally. Further studies to determine the precise structural relationship are underway.

One crystal with **C** {10} ↔ **G** {211} relationship was further tilted along the common $[1\ \bar{2}\ \bar{1}]_G/[10]_C$ axis. Typical contrast from $[311]_G$ (Figure 6a) to $[210]_G$ (Figure 6b) and then to $[53\ \bar{1}]_G$ (Figure 6c) appeared with tilting, while the contrast of **C** (marked by arrows) remained the same. It can be deduced that the channels of **C** are always parallel to the {211} planes of **G**; they are crystallographically related and grow epitaxially, which provides further experimental proof for the **C** {10} ↔ **G** {211} transition.

With an increase of Brij-56 concentration (Brij-56/C_{18}GluA molar ratio 1.45), we found that a novel SMC sphere with

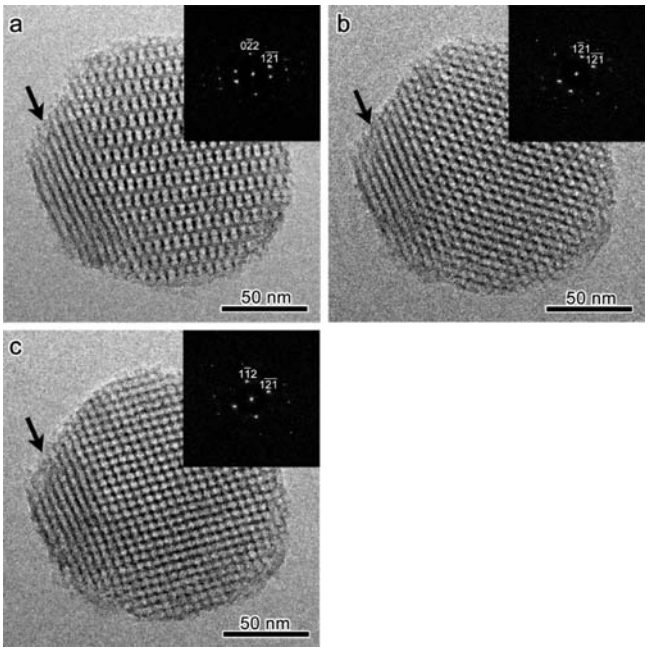

Figure 6. HRTEM images and the corresponding FDs of one particle with intergrowth of **C** and **G** tilting along the common $[1\,\bar{2}\,\bar{1}]_G/[10]_C$ axes: (a) $[311]_G$ direction, (b) $[210]_G$ direction, (c) $[53\,\bar{1}]_G$ direction.

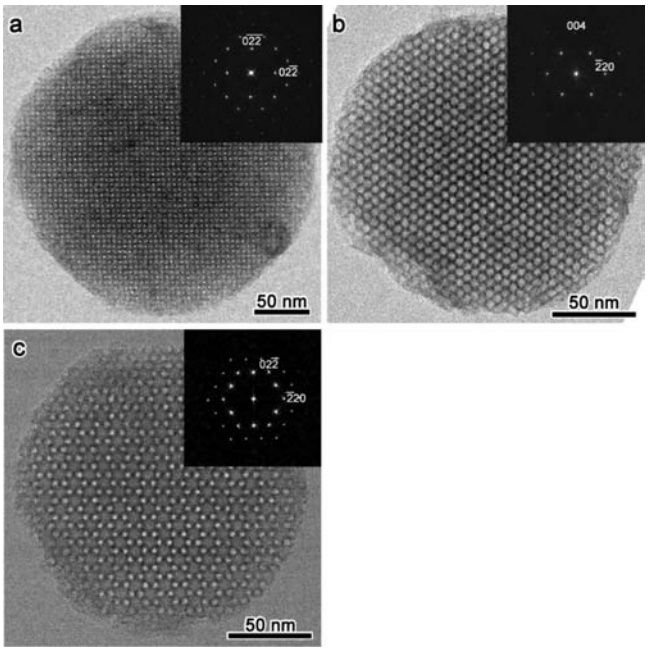

Figure 8. HRTEM images and the corresponding FDs of the sample synthesized with Brij-56/C_{18}GluA molar ratio of 1.75, taken along (a) [100], (b) [110], and (c) [111] axes.

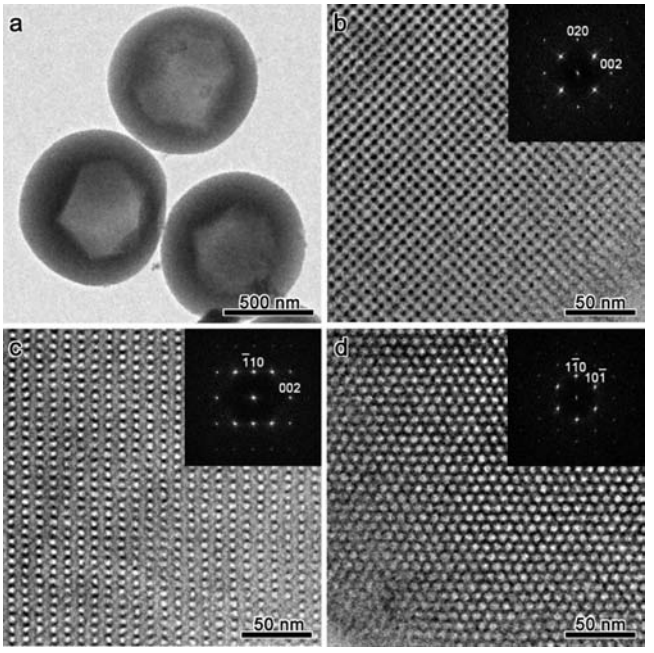

Figure 7. HRTEM images of the sample synthesized with Brij-56/C_{18}GluA molar ratio of 1.45, showing spherical shape with inner polyhedral cavity. (a) Low magnification TEM image, HRTEM images, and the corresponding FDs taken along (b) [100], (c) [110], and (d) [111] axes.

remarkable polyhedral (icosahedral, decahedral, Wulff polyhedral, and their partial combinations, Figure S8g) hollow morphology and a highly ordered **D** structure was formed in the shell region (Figure 7). Formation of the reverse multiply twinned particle (MTP) led to the icosahedral/decahedral hollow structure, and the Wulff polyhedral hollow structure was formed by **D** single crystal. The detailed structural solution and the formation mechanism study for this hollow crystal have been reported very recently.[44]

The sample synthesized with Brij-56/C_{18}GluA molar ratio 1.75 also showed spherical morphology with crystallographic facets (Figure S8i). Figure 8 shows the HRTEM images taken along the [100] (Figure 8a), [110] (Figure 8b), and [111] zone axes (Figure 8c), all of which show the typical contrast for **G** mesostructures. The samples synthesized with higher Brij-56/C_{18}GluA molar ratio showed similar mesostructure; however, impurities were obtained at higher Brij-56 concentration (not shown).

Nitrogen adsorption−desorption isotherms of these samples are shown in Figure S9, Supporting Information. All the samples show typical type IV isotherm with an evident hysteresis loop in the range of P/P_0 = 0.35−0.8. Their specific surface area, pore diameters, and pore volumes are listed in Table S2.

3.2. Mechanism of the Structural Transition. When the CSDA is used in the anionic surfactant system, the CSDA acts not only to link the silica species to the micelle surface but also to affect the surfactant packing. For ionic surfactants, the area of surfactant headgroup is strongly related to the dissociation of the headgroups and the ionic strength of the solution. The strong electrostatic attraction between the surfactant headgroup and the organic group of CSDA will favor a close packing of the surfactant and CSDA, therefore leading to a decrease in the area of the hydrophilic headgroup and an increase in the average packing parameter. This carboxylate−amine interactions and phase transitions have been have been thoroughly studied previously for asymmetric chain catanionic surfactant systems.[45−47] It has been reported that such cationic−anionic surfactant systems have been also applied to SMCs by adding anionic surfactants as cosurfactants in the cationic surfactant templating system.[48,49]

In this article, all the samples have been synthesized with a fixed APS/C_{18}GluA molar ratio of 2 to ensure 1:1 interaction between the diprotic glutamic surfactant headgroup and the CSDA. This essentially suggests that the active surfactant initially is the same in all cases, being an surfactant−CSDA complex, and the different structures obtained were induced by (a) the influence of the nonionic surfactant Brij-56 and (b) the condensation of charged silica species.

The experimental results show that the mesostructures with various organic/inorganic interface curvature can be tuned by the nonionic surfactant Brij-56, depending on the concentration and reaction temperature. It was observed that (I) the *d*-spacing of the as-synthesized samples with the same structure gradually increased with the addition of Brij-56, indicating that Brij-56 molecules were incorporated into the surfactant micelles. (II) The *g* parameter changed according to the amount of Brij-56 added, which also suggests that the Brij-56 molecules mixed with anionic surfactant and changed the packing behavior of the anionic surfactant. On the basis of these experimental data, the effect of Brij-56 on the formation of mesostructures can be explained in terms of the change in *g* parameter of the surfactant micelle by Brij-56 penetration.[43] It is well-known that the cloud point of Brij-56 is in the range 64−69 °C, and its hydrophobicity increases with increasing temperature caused by the destruction of the hydrogen bond between Brij-56 and H_2O.[50] The outer region of the nonionic surfactant micelle comprises coils of hydrated EO chains. At higher temperature, the structured water around the nonionic surfactant headgroup is excluded from the hydrophilic region, and EO−EO interactions became dominant over EO−water interactions, finally resulting in phase separation (cloud point).[51] Thus, at higher temperature the Brij-56 molecule becomes more hydrophobic and tends to be associated with the hydrophobic part of the anionic surfactant C_{18}GluA and increased the *g* parameter.

Thus, (I) at low temperature (30 °C), the anionic and nonionic surfactants form mixed micelles where the headgroups of both types of surfactants favor the aqueous region over the hydrophobic part, and the *g* parameter is increased; thus, **C** was formed instead of the cage-type structure. It was observed that the *d*-spacing of as-synthesized samples with **C** structure (Brij-56/C_{18}GluA = 0.29−1.75) gradually increased with addition of Brij-56, indicating that Brij-56 molecules were incorporated into the surfactant micelles (Figure S1 and Table S3, Supporting Information). (II) At 50 °C, the $(EO)_{10}$ part is partially hydrophobic and partially hydrophilic, and the $(EO)_{10}$ part can be in both the hydrophobic C_{18} part and the hydrophilic GluA part. More Brij-56 molecules can enter the C_{18} part, and thus *g* increases to form **C** and then bicontinuous structures. The *d*-spacing of the as-synthesized samples with **C** structure (Brij-56/C_{18}GluA = 0.29−0.85) and **G** structure (Brij-56/C_{18}GluA = 1.60−1.90) also increased gradually with the addition of Brij-56, suggesting that more Brij-56 molecules entered the surfactant micelles (Figure S7 and Table S3). (III) At 80 °C, which is over the cloud point of Brij-56, the Brij-56 molecules become highly hydrophobic and can dramatically increase the *g* parameter, leading to formation of **L** structure (Brij-56/C_{18}GluA = 1.45−1.75, Figure S4 and Table S3). (IV) It has been observed that the SMCs synthesized at higher temperature often show smaller *d*-spacings. Due to the facile thermal motion of the surfactant chain at higher temperatures, it can be imagined that the hydrophobic chain would coil easily to fill the space and thus maximize their van der Waals interactions, leading to lower total energy and the smaller pore size. However, Brij-56 molecules become more hydrophobic at higher temperature and increase the micelle size dramatically. Consequently, when Brij-56 molecules were added to the reaction mixture, samples with similar structure (Brij-56/C_{18}GluA = 0.29−0.85) showed increased *d*-spacing with increasing temperature (Table S3). (V) When a large amount of Brij-56 was added to the reaction solution, some Brij-56 molecules would have remained in the solution and outside the micelles, which disperses the nucleation sites and limits the diffusion of silicate oligomers in the synthesis of the nanoparticles, acting as a dispersant.[43] Thus, it can be considered that larger amounts of added Brij-56 and higher temperature facilitate the formation of mesostructures with a larger *g* parameter and low organic/inorganic interface curvature.

It should be also noted that the kinetics of SMC formation, especially the silica condensation, also changed with increasing temperature. It has been found that the surfactant packing is the dominant factor in determining the final structure of the SMCs, and the match between the interfacial charge density of the inorganic silica framework and the charge density of the surfactant headgroups affects the kinetics of the mesophase transition.[52,53] Traditionally, silica sources have opposite charges to the surfactant micelles (also metal/haloid counterion mediated); thus, the inorganic silicate walls have direct charge matching with the organic template. However, in the present case, the CSDA acts as a bridge, linking the surfactant and the silica source and thus hindering the charge matching of the silicate wall with the surfactant. During the condensation process of the silicate wall, the reduced negative charge density of the silicate network would enhance the interaction between the CSDA and the surfactant, driving the silica close to the micelle surface, and the organic surfactants would then pack to form mesostructures with higher organic/inorganic interface curvature with a lower *g* parameter.[44] Here, our results suggest that the *g* parameter of the mesostructures obtained with increasing reaction temperature became larger, contrary to the kinetic effect of the silica condensation. Thus, surfactant packing (thermodynamic control) is the dominant factor in determining the final mesostructure.

It can be concluded from the results obtained at 50 °C that the cage-type structure, which has the largest organic/inorganic interface curvature (ideally $g = 1/3$), was formed without addition of Brij-56. **C**, with organic/inorganic interface curvature (ideally $g = 1/2$) smaller than that of the cage-type structure, was formed in the zones with a moderate amount of Brij-56 due to the enlarged hydrophobic volume contribution to the packing parameter *g*. Increasing the ratio of Brij-56/C_{18}GluA led to the formation of bicontinuous minimal surface structures (**D** and **G**), which have lower organic/inorganic interface curvature (ideally $g = 2/3$), through the intergrowth regions (**C** and **D**, **C** and **G**). **L** was not obtained at 50 °C, because a viscous solution was formed at higher concentrations of Brij-56. However, with Brij-56/C_{18}GluA molar ratio 1.45−1.75, **C**, bicontinuous structures (**D** and **G**), and **L** were formed at 30 °C, 50 °C, and 80 °C, respectively. As noted above, the hydrophobicity of Brij-56 increases with increasing reaction temperature. Hence, it can be considered that **L** is the next structure, which has the vanished organic/inorganic interface curvature ($g = 1$). Thus, with increase of the *g* parameter and decrease of organic/inorganic interface curvature, mesostructures were formed in this system in the sequence cage-type → **C** → intergrowth of **C** and **D** → intergrowth of **C** and **G** → **D** → **G** → **L**. Notably, the mesostructure has a peculiar order such that the intergrowth of **D**/**G** and the pure **D**/**G** structures were formed alternately, and **G** always

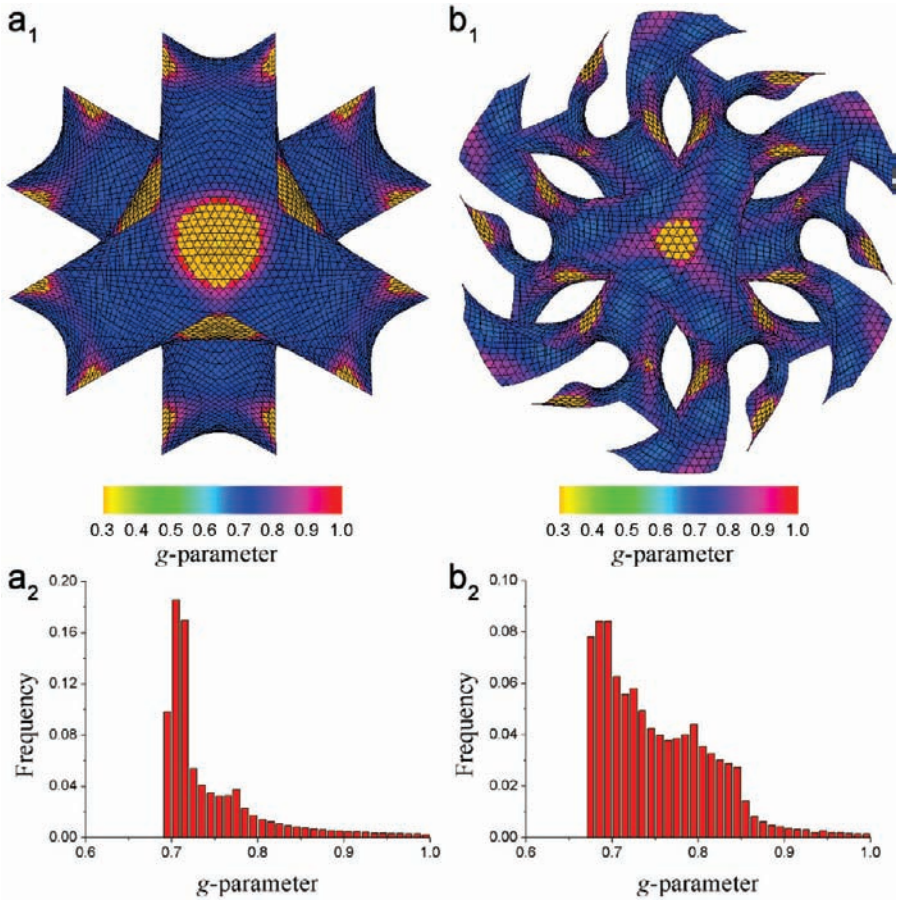

Figure 9. 3D reconstruction and actual *g* value distribution of the (a) **D** and (b) **G** structure.The local *g* parameters were obtained from the mean curvature and Gaussian curvature distributions on the equi-electrostatic potential surfaces according to the parallel surface concept.

appeared after **D** with increase of the mole fraction of Brij-56 in the synthesis system.

The *g* parameter relates the micellar global geometry to the molecular shape of surfactants and facilitates understanding of mesostructure formation. However, the *g* parameter is a qualitative measure based on ideal geometries. The *g* value of the bicontinuous structures (**D**, **G**, and **P**) has to be 2/3 when the mean curvature $H = 0$ everywhere, which means that all of those minimal surfaces must have this value. In the case of bicontinuous SMCs, the actual interface does not lie on the $H = 0$ surface (mean curvature > 0; thus, *g* is not 2/3) due to the thickness of the silicate wall. In an attempt to explain the fact that **D** appears prior to **G** with increasing amount of Brij-56, we evaluated the actual *g* value distribution over the actual interfaces of both **D** and **G** based on the experimental data. To do so, we adopted the electron crystallography (EC) reconstruction results (see Supporting Information for details of the reconstruction and the structure factor tables of **D** and **G**). Provided that an equipotential surface of EC properly represents the interface, the local *g* parameter can be obtained from the mean curvature and Gaussian curvature according to the parallel surface concept,[54] and consequently the averaged *g* value over the interface (termed $\langle g \rangle$) is also obtained. The values of $\langle g \rangle_{\mathbf{D}}$ and $\langle g \rangle_{\mathbf{G}}$ were calculated in the range $0 < g < 1$ to eliminate the calculation noise. The determined threshold of **D** was 75% out of the rescaled 0−100%, and that of **G** was 53% by minimizing the Helfrich energy density of the boundary (Figure 9).[35,54]

The actual *g* value distributions are color-coded on the equipotential surfaces of the **D** (Figure 9a_1) and **G** (Figure 9b_1) structures. The corresponding histograms are presented in Figure 9a_2 and 9b_2, respectively. In both cases, *g* exceeds the ideal value of 2/3 (for bicontinuous minimal surfaces) at most points of the interface (colored by blue), which suggests that the interface geometry is highly hyperbolic. The vicinity of the flat point is depicted in orange, and the interface is concave. The histograms of *g* values are both highly right-skewed, which mediates changes in the *g* value from the concave domain ($g \sim 0.3$, not shown in the histograms in Figure 9) to the hyperbolic domain ($g > 2/3$). From this result, considerable variation of the local surfactant molecular shape must occur around the flat points, leading to the deviating density distribution within the hydrophobic tail region. We speculate that for the present synthetic system, the additive Brij-56 can compensate for this density deviation, and eventually the system is stabilized, allowing formation of **D** and **G**. Within the hyperbolic range of $g > 2/3$ in Figure 9, *g* exhibits more homogeneous and sharper frequency distribution in **D**. On this basis, the averaged *g* for **D** is $\langle g \rangle_{\mathbf{D}} = 0.7261$, and that for **G** is $\langle g \rangle_{\mathbf{G}} = 0.7436$; thus $\langle g \rangle_{\mathbf{G}}$ is slightly higher than $\langle g \rangle_{\mathbf{D}}$ by ~0.02. This experimental result using EC confirms the following. Addition of Brij-56 is still effective for the bicontinuous mesostructures by decreasing the overall interfacial curvature. In this synthetic system, compared with **D**, **G** can afford more deviating curvatures on its interface, which leads to formation of **G** with a higher average of the *g* value distribution. Thus, it is reasonable

that in this synthesis, **G** appears closer to **L** and the similar *g* values of **D** and **G** make the structural change sequence complex, with many intergrowth structures.

4. CONCLUSIONS

Various mesostructures were synthesized in the AMS system by using an amino acid-derived anionic surfactant as the template in the presence of nonionic surfactant Brij-56. The mesostructures were determined by the organic/inorganic interface curvature, as Brij-56 with a noncharged headgroup tends to be associated with the anionic surfactant micelle and can penetrate the micelles and increase the hydrophobic volume. The synthesis-field diagram of the system shows the peculiar structural change sequence cage-type → **C** → intergrowth of **C** and **D** → intergrowth of **C** and **G** → **D** → **G** → **L**, with increase of the *g* parameter and decrease of organic/inorganic interface curvature. The local *g* parameter was obtained from the experimental data by calculating mean curvatures and Gaussian curvatures from the equi-electrostatic potential surface, and **G** and **D** were distinguished experimentally. Intergrowth of **C** and **D** and two kinds of intergrowth of **C** and **G** were discovered. These findings provide support for structural transformation by varying organic/inorganic interface curvature and will be useful in future mesostructure design and control of both SMC systems and liquid crystal mesophases. This subject will be of interest to researchers in diverse areas of chemistry, particularly those in inorganic, colloid, physical, and materials chemistry.

■ ASSOCIATED CONTENT

Supporting Information. XRD patterns, nitrogen adsorption-desorption, SEM and HRTEM images of the sample (synthesized at 30 °C, 80 °C, and 50 °C), the synthesis conditions, and electron crystallographic data. This material is available free of charge via the Internet at http://pubs.acs.org.

■ AUTHOR INFORMATION

Corresponding Author
chesa@sjtu.edu.cn

■ ACKNOWLEDGMENT

We thank Dr. Alfonso E. Garcia-Bennett and Dr. Toen Castle for fruitful scientific discussions. We acknowledge the support of the National Natural Science Foundation of China (Grant No. 20890121), the 973 project (2009CB930403) of China, and the WCU program (R-31-2008-000-10055-0) of South Korea. The microscopy works were supported by the (Knut and Alice) Wallenberg Foundation, Sweden and EXSELENT project, Sweden.

■ REFERENCES

(1) Sayari, A. *Chem. Mater.* **1996**, *8*, 1840.
(2) Van Rhijn, W. M.; De Vos, D. E.; Sels, B. F.; Bossaert, W. D.; Jacobs, P. A. *Chem. Commun.* **1998**, 317.
(3) Vallet-Regi, M.; Ramila, A.; Del Real., R. P.; Pérez-Pariente, J. *Chem. Mater.* **2001**, *13*, 308.
(4) Kresge, C. T.; Leonowicz, M. E.; Roth, W. J.; Vartuli, J. C.; Beck, J. S. *Nature* **1992**, *359*, 710.
(5) Huo, Q.; Margolese, D. I.; Stucky, G. D. *Chem. Mater.* **1996**, *8*, 1147.
(6) Firouzi, A.; Kumar, D.; Bull, L. M.; Besier, T.; Sieger, P.; Huo, Q.; Walker, S. A.; Zasadzinsky, J. A.; Glinka, C.; Nicol, J.; Margolesse, D.; Stucky, G. D.; Chmelka, B. F. *Science* **1995**, *267*, 1138.
(7) Israelachvili, J. N.; Mitchell, D. J.; Ninham, B. W. *J. Chem. Soc., Faraday Trans. 2* **1976**, *72*, 1525.
(8) Zhao, D.; Feng, J.; Huo, Q.; Melosh, N.; Fredrickson, G. H.; Chmelka, B. F.; Stucky, G. D. *Science* **1998**, *279*, 548.
(9) Tanev, P. T.; Pinnavaia, T. J. *Science* **1995**, *267*, 865.
(10) Huo, Q.; Margolese, D. I.; Ciesla, U.; Feng, P.; Gier, T. E.; Sieger, P.; Leon, R.; Stucky, G. D. *Nature* **1994**, *368*, 317.
(11) Kaneda, M.; Tsubakiyama, T.; Carlsson, A.; Sakamoto, Y.; Ohsuna, T.; Terasaki, O. *J. Phys. Chem. B* **2002**, *106*, 1256.
(12) Sakamoto, Y.; Kaneda, M.; Terasaki, O.; Zhao, D.; Kim, J. M.; Stucky, G. D.; Shin, H. J.; Ryoo, R. *Nature* **2000**, *408*, 449.
(13) Yu, C. Z.; Tian, B. Z.; Fan, J.; Stucky, G. D.; Zhao, D. *J. Am. Chem. Soc.* **2002**, *124*, 4556.
(14) Che, S.; Garcia−Bennett, A. E.; Yokoi, T.; Sakamoto, K.; Kunieda, H.; Terasaki, O.; Tatsumi, T. *Nat. Mater.* **2003**, *2*, 801.
(15) Gao, C.; Sakamoto, Y.; Sakamoto, K.; Terasaki, O; Che, S. *Angew. Chem., Int. Ed.* **2006**, *45*, 4295.
(16) Garcia−Bennett, A. E.; Kupferschmidt, N.; Sakamoto, Y.; Che, S.; Terasaki, O. *Angew. Chem., Int. Ed.* **2005**, *44*, 5317.
(17) Gao, C.; Sakamoto, Y.; Terasaki, O.; Che, S. *Chem.—Eur. J.* **2008**, *14*, 11423.
(18) Alfredsson, V.; Anderson, M. W. *Chem. Mater.* **1996**, *8*, 1141.
(19) Anderson, M. W.; Egger, C. C.; Tiddy., G. J. T.; Casci, J. L.; Brakke, K. A. *Angew. Chem., Int. Ed.* **2005**, *44*, 3243.
(20) Anderson, M. W.; Hughes, P. J.; Terasaki, O.; Sakamoto, Y.; Brakke, K. *Stud. Surf. Sci. Catal.* **2007**, *165*, 13.
(21) Jain, A.; Toombes, G. E. S.; Hall, L. M.; Mahajan, S.; Garcia, C. B. W.; Probst, W.; Gruner, S. M.; Wiesner, U. *Angew. Chem., Int. Ed.* **2005**, *44*, 1226.
(22) Rançon, Y.; Charvolin, J. *J. Phys. Chem.* **1988**, *92*, 6339. **1998**, *92*, 2646.
(23) Matsen, M. W. *Phys. Rev. Lett.* **1998**, *80*, 4470.
(24) Honda, T.; Kawakatsu, T. *Macromolecules* **2006**, *39*, 2340.
(25) Förster, S.; Khandpur, A. K.; Zhao, J.; Bates, F. S.; Hamley, I. W.; Ryan, A. J.; Bras, W. *Marcomolecules* **1994**, *27*, 6922.
(26) Wang, C. Y.; Lodge, T. P. *Macromolecules* **2002**, *35*, 6997.
(27) Vigild, M. E.; Almdal, K.; Mortensen, K.; Hamley, I. W.; Fairclough, J. P. A.; Ryan, A. J. *Marcomolecules* **1998**, *31*, 5702.
(28) Squires, A. M.; Templer, R. H.; Seddon, J. M. *Langmuir* **2002**, *18*, 7384.
(29) Squires, A. M.; Templer, R. H.; Seddon, J. M.; Woenkhaus, J.; Winter, R.; Narayanan, T.; Finet, S. *Phys. Rev. E.* **2005**, *72*, 011502.
(30) Conn, C. E.; Ces, O.; Squires, A. M.; Mulet, X.; Winter, R.; Finet, S. M.; Templer, R. H.; Seddon, J. M. *Langmuir* **2008**, *24*, 2331.
(31) Hyde, S. in *Handbook of applied surfaces and colloid chemistry*; Holmberg, K., Ed.; John Wiley and Sons: New York, 2001; Chapter 16.
(32) Gallis, K. W.; Landry, C. C. *Chem. Mater.* **1997**, *9*, 2035.
(33) Landry, C. C.; Tolbert, S. H.; Gallis, K. W.; Monnier, A.; Stucky, G. D.; Norby, P.; Hanson, J. C. *Chem. Mater.* **2001**, *13*, 1600.
(34) Garcia−Bennett, A. E.; Terasaki, O.; Che, S.; Tatsumi, T. *Chem. Mater.* **2004**, *16*, 813–821.
(35) Miyasaka, K.; Terasaki, O. *Angew. Chem., Int. Ed.* **2010**, *49*, 8867.
(36) Huo, Q.; Margolese, D. I.; Ciesla, U.; Demuth, D. G.; Feng, P.; Gier, T. E.; Sieger, P.; Firouzi, A.; Chmelka, B. F.; Schüth, F.; Stucky, G. D. *Chem. Mater.* **1994**, *6*, 1176.
(37) Che, S.; Garcia−Bennett, A. E.; Yokoi, T.; Sakamoto, K.; Kunieda, H.; Terasaki, O.; Tatsumi, T. T. *Nat. Mater.* **2003**, *2*, 801.
(38) Gao, C.; Qiu, H.; Zeng, W.; Sakamoto, Y.; Terasaki, O.; Sakamoto, K.; Chen, Q.; Che, S. *Chem. Mater.* **2006**, *18*, 3904.
(39) Garcia−Bennett, A. E.; Miyasaka, K.; Terasaki, O.; Che, S. *Chem. Mater.* **2004**, *16*, 3597–3605.

(40) Che, S.; Liu, Z.; Ohsuna, T.; Sakamoto, K.; Terasaki, O.; Tatsumi, T. *Nature* **2004**, *429*, 281–284.
(41) Gao, C.; Sakamoto, Y.; Terasaki, O.; Sakamoto, K.; Che, S. *J. Mater. Chem.* **2007**, *17*, 3591.
(42) Gao, C.; Che, S. *Adv. Funct. Mater.* **2010**, *20*, 2750.
(43) Han, L.; Chen, Q.; Wang, Y.; Gao, C.; Che, S. *Microporous Mesoporous Mater.* **2011**, *139*, 94.
(44) Han, L.; Xiong, P.; Bai, J.; Che, S. *J. Am. Soc. Chem.* **2011**, *133*, 6106.
(45) Regev, O.; Khan, A. *J. Colloid Interface Sci.* **1996**, *182*, 95.
(46) Eastoe, J.; Rogueda, P.; Shariatmadari, D.; Heenan, R. *Colloid Surface A* **1996**, *117*, 215.
(47) Silva, B. F. B; Marques, E. F.; Olsson, U. *Soft Matter* **2011**, *7*, 225.
(48) Chen, F.; Huang, L.; Li, Q. *Chem. Mater.* **1997**, *9*, 2685.
(49) Lind, A.; Spliethoff, B.; Lindén., M. *Chem. Mater.* **2003**, *15*, 813.
(50) Quina, F. H.; Hinze, W. L. *Ind. Eng. Chem. Res.* **1999**, *38*, 4150.
(51) Fong, C.; Weerawardena, A.; Sagnella, S. M.; Mulet, X.; Krodkiewska, I.; Chong, J.; Drummond., C. J. *Langmuir* **2011**, *27*, 2317.
(52) Tolbert, S. H.; Landry, C. C.; Stucky, G. D.; Chmelka, B. F.; Norby, P.; Handon, J. C.; Monnier, A. *Chem. Mater.* **2001**, *13*, 2247.
(53) Monnier, A.; Schuth, F.; Huo, Q.; Kumar, D.; Margolese, D.; Maxwell, R. S.; Stucky, G. D.; Krishnamurty, M.; Petroff, P.; Firouzi, A.; Janicke, M.; Chmelka, B. F. *Science* **1993**, *261*, 1299.
(54) Hyde, S. T.; Andersson, S.; Larsson, K.; Blum, Z.; Landh, T.; Lidin, S.; Ninham, B. W. *The Language of Shape*; Elsevier Science B.V.: Amsterdam, 1997; Chapter 4.